coatings

MDPI

Article

Adsorption Capability and Mechanism of Pb(II) Using MgO Nanomaterials Synthesized by Ultrasonic Electrodeposition

Dan Tang [1,2], Quanqing Zhang [1], Guanglei Tan [1,2,*], Lijie He [1,2,*] and Fafeng Xia [3]

[1] Liaoning Provincial Engineering Research Center for High-Value Utilization of Magnesite, Yingkou Institute of Technology, Yingkou 115014, China; tangdand121@163.com (D.T.); zhangqq12311@163.com (Q.Z.)
[2] Liaoning Provincial Key Laboratory of Energy Storage and Utilization, Yingkou Institute of Technology, Yingkou 115014, China
[3] College of Engineering, Northeast Agricultural University, Harbin 150030, China; xiaff@126.com
* Correspondence: gltan1979@163.com (G.T.); helijie@yku.edu.cn (L.H.)

Abstract: This work describes the process of synthesizing magnesia (MgO) nanomaterials through ultrasonic electrodeposition, followed by an examination of their ability and mechanism to remove Pb(II) from industrial soil at 100, 150, and 200 W ultrasonic powers. Nanomaterials were examined for their surface shape and phase composition using scanning electron microscopy (SEM), transmission electron microscopy (TEM), and X-ray diffractometry (XRD). The capability of magnesia nanomaterials to adsorb Pb(II) improved greatly when operated at 150 W, attaining a maximal 68.94 mg/g value. Adsorption of Pb(II) onto magnesia nanomaterial surfaces was examined by utilizing the pseudo-second-order kinetic and Langmuir models. The nanomaterials exhibited significant features of both chemical and monolayer adsorptions for Pb(II) as a result of the intense chemical interactions between the atoms of the magnesia nanomaterials' surface and Pb(II), as shown by Fourier transform infrared (FTIR) analysis. At 30 °C, the magnesia nanomaterial exhibited the highest adsorption capacity for Pb(II), suggesting that temperature played a significant role in this capacity. Furthermore, the Langmuir model produced a correlation coefficient greater than 0.99, indicating an excellent fit for the adsorption behavior of magnesia towards Pb(II). The findings suggest that ultrasonic power significantly impacts the adsorption characteristics of magnesia nanoparticles synthesized via ultrasonic electrodeposition. Specifically, ultrasonic power of 150 W yields the most efficient adsorption characteristics. Moreover, the 150 W-fabricated magnesia materials demonstrated exceptional pH compatibility.

Keywords: microstructure; adsorption capability; MgO nanomaterial; ultrasonic power; lead ion

check for updates

Citation: Tang, D.; Zhang, Q.; Tan, G.; He, L.; Xia, F. Adsorption Capability and Mechanism of Pb(II) Using MgO Nanomaterials Synthesized by Ultrasonic Electrodeposition. *Coatings* **2024**, *14*, 891. https://doi.org/10.3390/coatings14070891

Academic Editor: Aivaras Kareiva

Received: 10 June 2024
Revised: 10 July 2024
Accepted: 15 July 2024
Published: 17 July 2024

1. Introduction

Lead (Pb)-contaminated soils contain high levels of Pb due to excessive industrial activity; this causes the metal to continuously release into the soil. Pb-contaminated soils contain various substances, including elevated heavy metal concentrations including arsenic, mercury, and chromium, as well as organic contaminants, organic matter, and soil minerals [1–3]. The incorporation of raw heavy metals into the natural environment has the potential to disrupt the ecosystem's equilibrium, reduce biodiversity, and harm soil fertility. Furthermore, hazardous heavy metal accumulation in the food chain can lead to significant health consequences for humans, such as cancer, neurological impairment, and reproductive problems. The element Pb is assigned the atomic number 80 on the periodic table. Soils often contain Pb in two distinct oxidation states: Pb(II) and Pb(IV). The compounds containing Pb compounds are generally extremely stable, resistant to natural decomposition, and can persist for long periods in the environment. Pb is a toxic heavy metal that has detrimental effects on the environment and human well-being. These compounds inhibit the reproduction and growth of aquatic and soil species in the environment. Prolonged exposure to high amounts of Pb (above values of 9 μg/L) can lead to anemia, renal failure, infertility, and problems with reproduction. Pb, due to its neurotoxic properties, poses significant risks to children. Excessive intake might result in behavioral problems, cognitive impairment, and difficulties in learning. However, the effective removal of Pb ions from soil is a significant environmental issue [4].

Various methods can be used to remove Pb ions, such as adsorption, membrane separation, reverse osmosis, chemical precipitation, and ion exchange. Adsorption offers numerous benefits, such as simplicity, selectivity, adaptability, cost-effectiveness, high efficiency, and environmental friendliness. As a result, adsorption has emerged as the preferred method for extracting Pb ions from soil. To eliminate Pb ions from the liquid solution, Zhao et al. [5] examined the Pb(II) adsorption characteristics of cellulose membranes across a variety of adsorption parameters. The influence of varying durations of contact on the Pb(II) adsorption performance obtained from wastewater using hydroxyapatite and $CoFe_2O_4$ was studied by Desalegn et al. [6]. To assess the removal of Pb(II) using chitosan–calix resorcinarene, Santoso tested the adsorption efficacy across a range of pH values, concentrations, and contact times.

Currently, a wide range of adsorbents has been effectively developed, such as metal-organic frameworks (MOFs), clay minerals, polymeric adsorbents, and biochar [7]. Although these adsorbents can eliminate impurities from water, their practical use is limited due to their inefficiency, time-consuming regeneration methods, and high cost. These drawbacks severely limit the potential growth and widespread application of adsorbents in the removal of heavy metal ions. Magnesite is a naturally occurring mineral composed of magnesium oxide (magnesia), an inorganic metal oxide with alkaline properties. Magnesia has various beneficial properties, such as increased specific surface area, excellent chemical and thermal stability, low solubility, and porous structure. Magnesia is a superior adsorbent compared to traditional materials like zeolite and activated carbon due to its ability to adjust its structure, durability, high stability, ease of regeneration and recovery, and pH adaptability. Tomishige et al. [8] examined the adsorption capability of magnesia for CO_2 at various loading levels using a fixed-bed reactor. The results demonstrated that with an increase in magnesia loading, the capacity of magnesia-RHA to absorb CO_2 initially rose and then declined. The possible environmental uses of Ag/MgO nanocomposite materials were studied by Jayapriya et al. [9]. Due to its extensive variety of uses, magnesia demonstrates significant potential as an adsorbent material. Apart from its application in adsorption, it is also utilized in diverse other fields such as flame retardancy, catalysis, and building materials.

Several strategies have been implemented to generate magnesia nanomaterials, including high-pressure and temperature hydrothermal synthesis, calcination at elevated temperatures with Mg salts, chemical precipitation of Mg salts with strong bases, and electrochemical processes. Electrochemical methods are exceptional in their capacity to operate at lower temperatures than other methods [10–12]. They are known for their security and dependability, as well as their exceptional energy efficiency and precise control. Ultrasonic electrodeposition is a method that uses ultrasonic vibrations in an electrolyte solution to deposit materials through an electrolytic reaction onto a conductive substrate. Ultrasound is used to promote ion migration, improve particle dispersion, increase the homogeneity and cohesion of the deposited layer, and minimize the presence of bubbles and contaminants [13,14]. Ultrasonic electrodeposition is more efficient than traditional electrodeposition procedures, resulting in materials of higher quality and improved properties. Liu et al. [15] investigated the properties and microstructure of nanostructured MnO_2 films made by ultrasonic electrodeposition for use in capacitors. Akbarpour et al. [11] examined the impacts of pulsed electrodeposition with ultrasonic assistance on various graphene/NiCo composite coating characteristics such as microhardness, surface roughness, microstructure, and electrochemical properties. Rajput et al. [16] developed microstructures with various grain sizes by ultrasonic spray electrodeposition. In order to improve the mechanical characteristics of the synthetic microstructures, they implemented grain size control. Few studies have examined the correlation between the production of magnesia adsorbents through ultrasonic electrodeposition and the various ultrasonic powers. Further investigation is necessary to determine the effects of ultrasonic power on the adsorption efficacy and microstructural characteristics of magnesia.

In this report, magnesia nanomaterial coatings were deposited onto 304 stainless steel substrates using ultrasonic electrodeposition. The ultrasonic power level was adjusted to investigate the impact of ultrasonic power on nanomaterials. The phase composition and surface topology of the prepared nanomaterials were assessed using XR (X-ray diffraction), SEM (scanning electron microscopy, FEG450, FEI Company, Hillsboro, OR, USA), and TEM (transmission electron microscopy, Libra120, Zeiss Company, Oberkauheng, Baden-Württemberg, Germany). The porosity and specific surface area were analyzed using the Brunauer–Emmett–Teller (BET) technique. Moreover, the mechanism of removing Pb ions by magnesia nanomaterial was studied using pseudo-second-order kinetic (PSOK) and Langmuir models.

2. Experiment

2.1. Materials and Instruments

The required reagents for this study include boric acid (H_3BO_3), sodium dodecyl sulfate ($C_{12}H_{25}SO_4Na$), potassium hydroxide (KOH), hydrochloric acid (HCl), magnesium chloride ($MgCl_2$), sodium acetate ($CH_3COONa \cdot 3H_2O$), magnesium sulfate heptahydrate ($MgSO_4 \cdot 7H_2O$), and lead nitrate ($Pb(NO_3)_2$). The particles and reagents used were of analytical quality and were obtained from Shanghai Yaoyi Material Co., LTD. A plating solution was prepared using ultrapure water (18.25 MΩ·cm). The following equipment was used in the current study: electrochemical workstations, ion benchtop meter, water baths, three-electrode systems, ultrasonic cleaners, pulsed power supplies, vacuum drying ovens, muffle furnaces, electrolytic cells, porosity analyzers, electronic balances, surface area, and pH meter. In addition, TEM, XRD, and SEM were used for imaging and analysis.

2.2. Synthesis of Magnesia Nanomaterials

The adhesion and uniformity of the coating were improved by performing cathodic pre-treatment on 304 stainless steel before the experiment. First, dust, oil, and other impurities were removed from the substrate surface using ethanol. The substrate was then mechanically polished to provide a rougher surface to increase the surface area and coating adhesion. The importance of mechanical polishing in optimizing the roughness factor for the coating has been well-documented. Polishing enhances the surface roughness, which is critical for achieving uniform coating adhesion and improved adsorption efficiency. Studies have shown that substrates with a controlled roughness factor exhibit better coating properties and higher adsorption capacities due to increased surface area and active sites availability [17]. The substrate was mechanically polished using a polishing machine equipped with silicon carbide abrasive papers of varying grits (400, 800, 1200, and 2000). The polishing was done manually in a sequential manner starting from the coarser to the finer grits to achieve a smooth surface finish. The final roughness value (Ra) was measured using a surface profilometer and found to be approximately 0.2 µm. This level of roughness was chosen to ensure consistent and reproducible results across all experiments. In order to increase the bonding between the substrate and the coating, weak acids were used to activate the substrate. Subsequently, the substrate underwent meticulous drying in a vacuum thermostatic oven to avoid any leftover moisture interfering with the electrodeposition process. Magnesia nanomaterial was synthesized using a three-electrode setup, with 304 stainless steel, saturated calomel, and a platinum plate as the working, reference, and counter electrodes, respectively. The experimental setup for depositing the magnesia nanomaterials is illustrated in Figure 1. Before being introduced into the electrolysis cell, the reagents were carefully calculated and completely dissolved in 500 mL of ultrapure water (H_2O). The power supply was turned on for the electrodeposition experiments, and the plating solution's specific composition is illustrated in Table 1. To speed up the deposition process, ultrasonic waves of varying powers were implemented in the electrodeposition experiment. The experimental procedure parameters are listed as follows: the plating bath temperature was 60 °C, the plating current density was 3 A/dm^2, the duty cycle was 15%, the pulse frequency was 50 Hz, and the ultrasonic power was 100~200 W. The current profile during electrodeposition was monitored, showing a stable current density of 3 A/dm^2 throughout the process. The faradic efficiency, calculated based on the deposited mass and theoretical mass, was found to vary with different ultrasonic power levels. Specifically, the faradic efficiencies were approximately 85%, 90%, and 88% for ultrasonic powers of 100 W, 150 W, and 200 W, respectively. The highest efficiency at 150 W indicates optimal energy utilization and deposition conditions at this power level. The electrochemical and chemical processes occurring at the cathode during the deposition of magnesia involve the reduction of magnesium ions and the formation of magnesia (MgO) through a series of reactions. The main reactions can be described as shown in Equations (1) and (2):

$$\mathrm{Mg} + \mathrm{H_2O} \rightarrow \mathrm{Mg(OH)_2} \tag{1}$$

$$\mathrm{Mg(OH)_2} \rightarrow \mathrm{MgO} + \mathrm{H_2O} \tag{2}$$

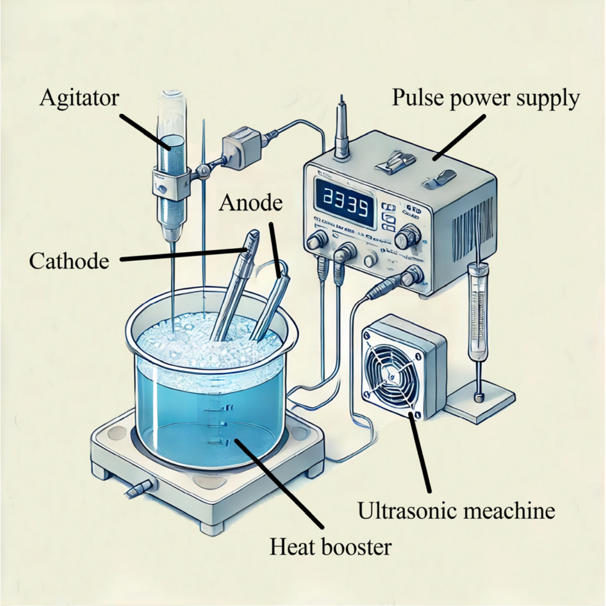

Figure 1. Experimental setup for depositing MgO nanomaterials.

Table 1. Specific composition of the plating solution.

Items (g/L)	Parameters
$MgSO_4 \cdot 7H_2O$	23~96
$MgCl_2$	66
H_3BO_3	16
KOH	28
$C_{12}H_{25}SO_4Na$	0.2
HCl	10
$CH_3COONa \cdot 3H_2O$	10
$Pb(NO_3)_2$	0.1

During the electrodeposition process, Mg^{2+} ions in the solution are reduced at the cathode to form metallic magnesium. This metallic magnesium can then react with water to form magnesium hydroxide ($Mg(OH)_2$), which upon dehydration during the heating process converts to magnesia (MgO). Ultrasonic treatment significantly affects the kinetics of these processes. The application of ultrasonic waves leads to cavitation, which generates localized high temperatures and pressures, enhancing the mass transfer and reaction rates at the electrode surface. The combination of these effects leads to a significant enhancement in the quality and properties of the MgO coatings deposited with ultrasonic assistance. Therefore, the use of ultrasonic treatment in the electrodeposition process is crucial for achieving high-performance magnesia nanomaterials with desirable properties.

The thickness of the MgO coating was measured using a profilometer, and it was found to vary with different ultrasonic power levels. Specifically, the coating thicknesses were approximately 2.5 µm, 3.1 µm, and 2.7 µm for ultrasonic powers of 100 W, 150 W, and 200 W, respectively. The optimal thickness observed at 150 W can be attributed to the improved particle dispersion and uniform deposition at this power level. After the experiment, the precursor was taken off the substrate and subjected to a 2 h heating in a muffle furnace after electrodeposition at 750 °C. Subsequently, it was gently cooled in a furnace until it reached room temperature (RT).

2.3. Adsorption Experiment

An extensive analysis was performed to assess the impact of several parameters, including initial temperatures, concentrations of Pb ions, and ultrasonic power, on the Pb ion adsorption capacity of magnesia coatings. In this study, humic acid and kaolinite were used as representative organic matter and clay minerals, respectively. Specifically, 0.01 g of humic acid and 0.01 g of kaolinite were incorporated into the Pb-loaded solution to reproduce an authentic scenario of Pb-contaminated soil. Small amounts of organic matter and clay minerals were incorporated into the Pb-loaded solution to reproduce an authentic scenario of Pb-contaminated soil. In addition, Pb solutions were prepared at various temperatures and concentrations. Using HCl and KOH, the pH was brought to the required level. After heat treatment, the magnesia material (0.01 g) was measured and then transferred to a conical flask. It was then mixed with 20 mL of a simulated Pb solution while agitated at 200 rpm and 30 °C for a specific duration. Following that, centrifugal solid–liquid separation was employed to separate the transparent supernatant. The concentration of Pb(II) in the supernatant was measured using a Pb ion electrode, enabling the assessment of its adsorption characteristics in various settings. The concentration of Pb(II) in the solution was measured using inductively coupled plasma optical emission spectroscopy (ICP-OES). Equation (3) was employed to calculate the adsorption capacity at equilibrium.

$$\mathrm{Q_e} = (\mathrm{C_0} - \mathrm{C_e}) \times \mathrm{V/m} \tag{3}$$

where Q_e is the number of metal ions adsorbed per unit amount of adsorbents (mg/g), C_0 and C_e represent the initial and equilibrium Pb(II) concentrations (mol/L), V represents the Pb(II) volume (L), and m represents the dry weight of adsorbents (g).

2.4. Characterization

The microstructure and surface morphology of magnesia nanomaterials were examined using SEM (FEG450, FEI Company, Hillsboro, OR, USA) and TEM (Libra120, Zeiss Company, Oberkauheng, Baden-Württemberg, Germany). The phase composition and structure of magnesia nanomaterials were analyzed using XRD (Ynamic500, Anton Paar Company, Graz, Stylmark, Austria). The wavelength, scanning speed, and angle range (2θ) of the Cu Kα radiation X-ray source were 1.5418 nm, 20°–90°, and 0.02°/s, respectively. Equation (4) was used to evaluate the RTC for the crystal orientation (hkl). Furthermore, the Scherrer formula was utilized to assess the MNN grain size.

$$\mathrm{RTC} = (\mathrm{I_{c(hkl)}}/\mathrm{I_{s(hkl)}})/\sum(\mathrm{I_{c(hkl)}}/\mathrm{I_{s(hkl)}}) \times 100\% \tag{4}$$

where $Ic(hkl)$ and $Is(hkl)$ represent the (hkl) plane diffraction intensities and standard nickel particles, respectively (JCPDS no. 04-0850).

3. Results and Discussion

3.1. Surface Morphology

The structural properties and surface topology of magnesia were studied using SEM images acquired for different ultrasonic power levels. Figure 2 shows SEM images of magnesia nanomaterials produced via ultrasonic electrodeposition. At 100 W (Figure 2a), the microstructure exhibits particle aggregation and a non-uniform distribution of large particles. At 150 W (Figure 2b), the particles are more evenly distributed, smaller, and form a porous structure, indicating effective dispersion. At 200 W (Figure 2c), the magnesia nanomaterial is dispersed, but the grain size is considerably greater with noticeable aggregation in certain areas. The average grain sizes were measured to be approximately 50 nm, 30 nm, and 60 nm for ultrasonic powers of 100 W, 150 W, and 200 W, respectively.

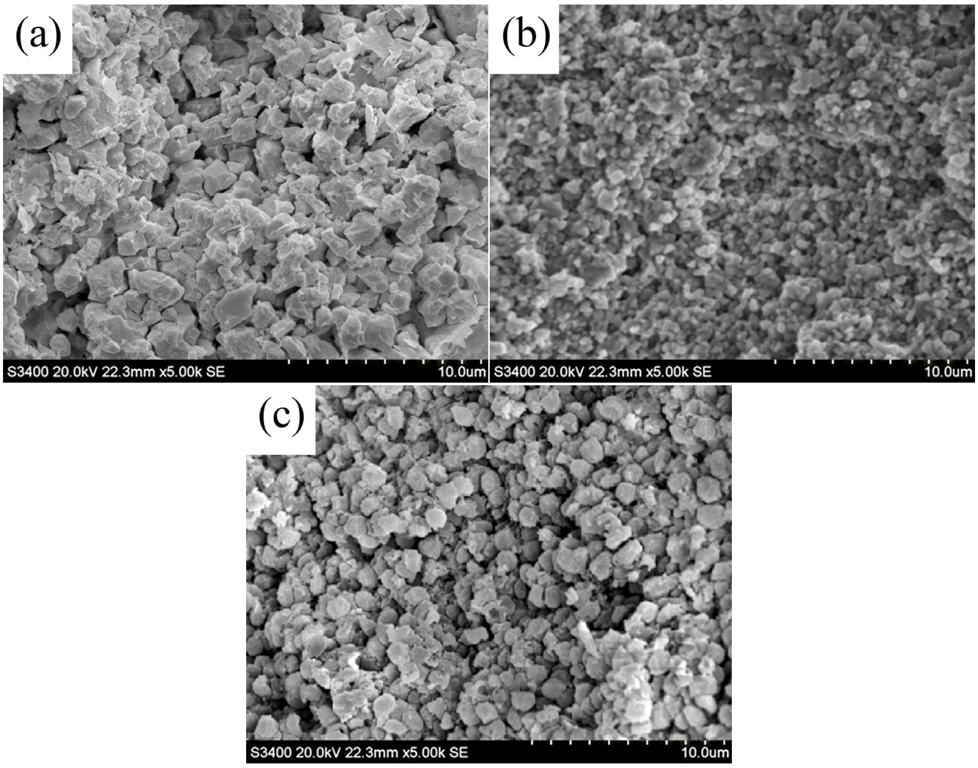

Figure 2. SEM pictures of MgO nanomaterials deposited at: (**a**) 100 W, (**b**) 150 W, and (**c**) 200 W.

When compared to coatings deposited without the use of ultrasound, significant differences were observed. Without ultrasonic treatment, the coatings exhibited much larger grain sizes, poor dispersion, and increased particle agglomeration, leading to a non-uniform and less porous structure. The average grain size in coatings deposited without ultrasound was approximately 100 nm, which is significantly larger than those obtained with ultrasonic power, particularly at 150 W. This comparison highlights the crucial role of ultrasonic power in refining the grain size and enhancing the uniformity and porosity of the coatings.

Different ultrasonic powers have a substantial influence on the final structure and synthesis of the material, resulting in microstructure changes [18]. At 150 W ultrasonic power, the cavitation effect of ultrasonic waves significantly increases the local pressure and temperature, which promotes the formation of numerous microbubbles. These microbubbles implode violently, causing high-speed jets and shock waves that enhance the diffusion of ions and particles in the electrolyte. This process leads to a more uniform and finer grain structure due to improved nucleation and reduced growth rates of the grains. Additionally, the enhanced mixing and dispersion at 150 W prevent particle aggregation and promote homogeneous particle distribution, resulting in smaller and more evenly distributed grains. At 100 W ultrasonic power, the cavitation impact of ultrasonic waves does not appreciably increase shear, pressure, or local temperature. This causes uneven particle aggregation and development, which impedes diffusion and uniform particle deposition. Supersaturation caused by 100 W power makes certain electrolyte regions more conducive to particle growth, resulting in larger and more irregularly distributed particles. At 150 W, ultrasonic waves achieve thermal and dynamic equilibrium, effectively dispersing particles via cavitation without producing excessive localized heat. This promotes homogeneous particle growth and diffusion, which is made possible by electrolyte micro-mixing. As a result, grain size becomes smaller and more evenly distributed. However, at 200 W, the electrolyte overheats in certain places due to the significant thermal effect, which accelerates grain development and promotes agglomeration. Elevated temperatures promote secondary grain formation, leading to reagglomeration.

3.2. Phase Composition

Figure 3 shows the magnesia nanomaterials' XRD patterns produced at different ultrasonic power levels. XRD analysis was performed to identify the crystalline phases present in the synthesized magnesia nanomaterials. The XRD patterns for the samples are shown in Figure 3. Reference peaks for MgO (JCPDS card No. 45-0946) and $Mg(OH)_2$ (JCPDS card No. 44-1482) were added to both Figure 3a,b. These materials exhibit a face-centered cubic (FCC) crystal structure, where each Mg atom is surrounded by an octahedral arrangement of O atoms, forming a cubic structure. Likewise, each O atom is arranged octahedrally with the Mg atoms, resembling the rock salt structure commonly found in various halides and oxides. The diffraction peaks at 63.23°, 42.88°, and 36.81° correspond to the (220), (200), and (111) crystal faces of the FCC structure of magnesia, respectively. Interestingly, at 150 W, the diffraction peaks appear wider and shorter compared to those under other conditions. The Scherrer equation indicates a negative correlation between grain size and diffraction peak width, suggesting that at 150 W, ultrasonic assistance results in decreased grain size. Furthermore, it enhances the dispersion of crystal orientation, resulting in a more randomly oriented grain structure [19]. Consequently, the diffraction peaks become wider. The diffraction peaks at 36.81°, 42.88°, and 63.23° correspond to the (111), (200), and (220) crystal faces of the FCC structure of magnesia (MgO), respectively, according to the JCPDS card No. 45-0946.

Figure 3b shows the XRD spectra of magnesia nanomaterials after adsorption, indicating a shift in diffraction angles to 18.77°, 34.72°, and 51.05°, respectively. These peaks correspond to the (002), (101), and (102) planes of $Mg(OH)_2$, according to the JCPDS card No. 44-1482. Comparing with JCPDS card 00-007-0239 demonstrates the transition of magnesia nanomaterials to $Mg(OH)_2$, which corresponds to crystallographic planes (102), (101), and (102). In addition, after adsorption at 150 W, weaker signals at 64.52°, 44.48°, and 31.19° were identified as Pb, contrary to JCPDS card 4-0686. However, magnesia samples produced at other ultrasonic powers did not contain elemental Pb. This is due to the higher Pb ion abundance at 150 W, which promotes the formation of larger Pb crystals on the surface. The observed $Mg(OH)_2$ peaks are slightly shifted compared to the standard values, suggesting lattice strain or defects in the structure.

The slight differences between the calculated and standard lattice constants indicate minor lattice distortions or imperfections in the synthesized materials.

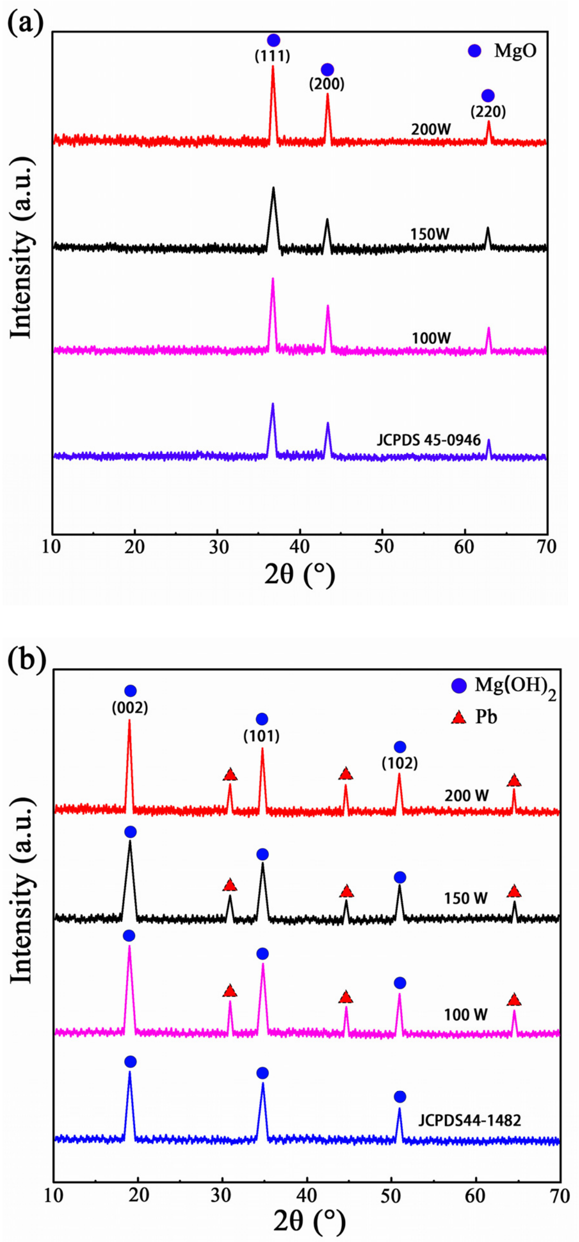

Figure 3. XRD patterns of MgO nanomaterials produced at different ultrasonic power levels: (**a**) before-adsorption, (**b**) post-adsorption.

3.3. TEM Analysis

Magnesia nanomaterials synthesized at 150 W were subjected to TEM investigation to elucidate their microstructural organization (Figure 4). The SEM results (Figure 4a) confirm the uniform magnesia dispersion, with 300 nm average diameter. An image acquired through a high-resolution TEM (Figure 4b) reveals the presence of pores between magnesia particles, indicating a mesoporous structure in materials synthesized via ultrasonic electrodeposition. The lattice growth direction (111) and lattice constant of 0.31 nm are depicted in Figure 4c. In Figure 4d, the selected area electron diffraction (SAED) pattern illustrates distinctly bright the polycrystalline nature of the magnesia nanomaterial synthesized at 150 W. The diffraction planes corresponding to the (111), (200), and (220) crystallographic orientations are consistent with the growth directions detected in XRD.

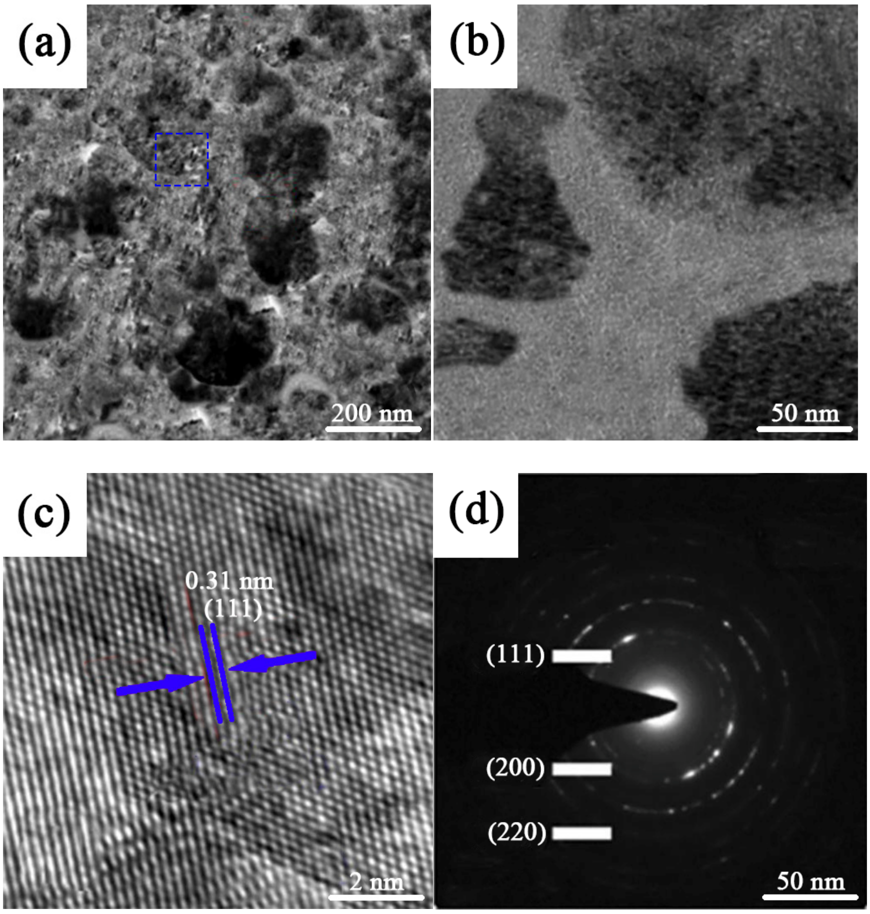

Figure 4. TEM analysis of MgO nanomaterials synthesized at 150 W ultrasonic power: (**a**) TEM image showing uniform dispersion with an average diameter of 300 nm; (**b**) high-resolution TEM image indicating a mesoporous structure; (**c**) lattice fringe image showing the (111) plane with a lattice constant of 0.31 nm; (**d**) SAED pattern with diffraction spots corresponding to the (111), (200), and (220) planes.

3.4. BET Analysis

Nitrogen adsorption tests were conducted at 150 W to examine the pore structure of the magnesia nanomaterials. The nitrogen adsorption–desorption isotherm in Figure 5a had a slightly uneven surface at lower relative pressures, indicating a limited microporous structure. With a rise in relative pressure, capillary condensation occurred, which resulted in the emergence of a clear hysteresis loop between adsorption and desorption. These properties are consistent with H4-type hysteresis loops and Type IV adsorption isotherms, indicating slit-like or mesoporous pores in the magnesia nanoparticles.

The pore size distribution curve of the magnesia nanomaterials produced at 150 W (Figure 5b) exhibited a range of sizes between 35 and 100 nm, with a calculated 90.12 cm^3/g of BET-specific surface area.

Surface areas for samples at 100 W and 200 W were 69.83 cm^3/g and 74.62 cm^3/g, respectively. This demonstrates that increasing the ultrasonic power from 100 W to 150 W significantly improves the specific surface area of magnesia, resulting in a more uniformly dispersed nanomaterial. However, a further increase in ultrasonic power to 200 W resulted in a decrease in BET-specific surface area. This reduction can be attributed to the excessive local heating and intense cavitation effects at higher ultrasonic power, which lead to the aggregation of particles and the formation of larger grains. These larger grains reduce the overall surface area available for adsorption. Therefore, while moderate ultrasonic power enhances the dispersion and specific surface area, excessive ultrasonic power has the opposite effect, promoting grain growth and reducing the surface area [20–22]. Thus, the optimal ultrasonic power for maximizing the BET-specific surface area is identified at 150 W, where the balance between particle dispersion and grain size is achieved without excessive aggregation.

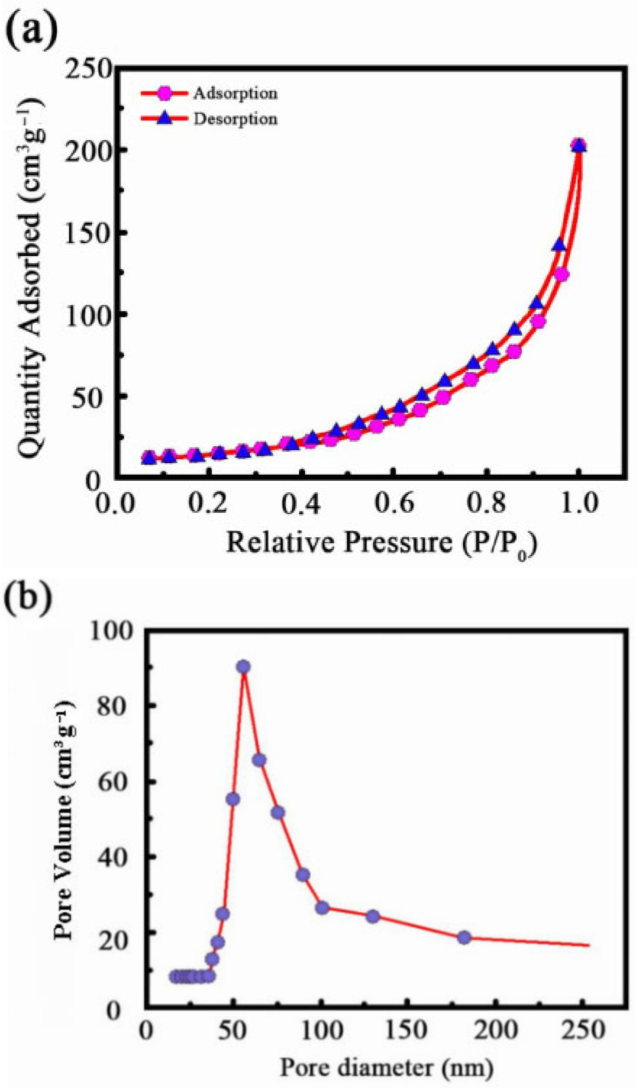

Figure 5. Nitrogen adsorption tests conducted at 150 W: (**a**) nitrogen adsorption–desorption isotherm, (**b**) pore size distribution.

When compared to coatings deposited without ultrasonic treatment, the BET-specific surface area of coatings deposited with ultrasound is significantly higher. Coatings deposited without ultrasound had a BET-specific surface area of approximately 50 cm^3/g, which is substantially lower than those deposited with ultrasonic assistance. This difference further underscores the beneficial impact of ultrasound in enhancing the porosity and specific surface area of the coatings.

The BET adsorption isotherms were also analyzed in their linear form. The BET equation can be expressed as Equation (5):

$$\frac{1}{\mathrm{V}(\frac{\mathrm{P_0}}{\mathrm{P}}-1)}=\frac{1}{\mathrm{V_m}}+(\frac{\mathrm{C}-1}{\mathrm{V_m C}})\frac{\mathrm{P}}{\mathrm{P_0}} \quad (5)$$

where V is the volume of adsorbed nitrogen gas, P is the equilibrium pressure, P_0 is the saturation pressure of nitrogen gas, V_m is the monolayer adsorbed gas volume, and C is the BET constant.

From the linear plots of $\frac{1}{V(\frac{P_0}{P}-1)}$ against $\frac{P}{P_0}$, we obtained the BET surface area and the constant *C*. The influence of ultrasound on these parameters is significant. At 100 W, the BET constant *C* and surface area were relatively low, indicating less favorable adsorption conditions. At 150 W, the constant *C* increased, and the surface area was maximized, indicating optimal adsorption conditions and a highly porous structure. At 200 W, both C and the surface area decreased, suggesting that the excessive ultrasonic energy led to partial collapse of the porous structure and particle agglomeration.

3.5. Adsorption Kinetics

Pb(II) adsorption kinetics on magnesia nanomaterials were analyzed using pseudo-second-order kinetics (PSOK) and pseudo-first-order kinetics (PFOK) models. Table 2 depicts the particular kinetic data and their corresponding findings. This work examined the adsorption capability of magnesia nanoparticles generated at pH 6.0 under different ultrasonic power levels over time. Pb(II) concentrations were initially set at 50 mg/L and the experiments were conducted at 30 °C.

Table 2. Calculate the lattice constant and standard value at 200W power.

Material	Plane (hkl)	2θ (Degress)	d-Spacing Å	Calculated Lattice Constant Å)	Standard Lattice Constant Å)
MgO	(111)	36.81	2.44	4.11	4.21
MgO	(200)	42.88	2.11	4.26	4.21
MgO	(220)	63.23	1.47	4.23	4.21
$Mg(OH)_2$	(002)	18.77	4.72	4.72	4.71
$Mg(OH)_2$	(101)	34.72	2.58	3.67	3.62
$Mg(OH)_2$	(102)	51.05	1.79	3.62	3.62

As illustrated in Figure 6, the Pb(II) removal by magnesia nanomaterials increased over time, with a rapid rise in adsorption from 0 to 60 min, then a gradual decline until equilibrium was achieved; however, it decreased with lower ultrasonic power. The optimal duration for adsorption was found to be 4 h, considering the reaction's efficacy. The primary explanation for the increase in Pb(II) adsorption by nanomaterials was the existence of surface vacant active sites, which facilitated rapid adsorption. Additionally, the increased specific surface area produced more active adsorption sites for Pb(II). Furthermore, the rate of adsorption decreased as Pb(II) occupied more active sites during the adsorption process, and eventually, saturation was reached. This site saturation affects the diffusion mechanism, causing Pb(II) to diffuse more slowly into the deeper or internal pores of the nanomaterial [23]. Consequently, after reaching saturation, the adsorption eventually slows down and comes to an end.

The data fitting using PFOK and PSOK models showed that the correlation coefficient (R^2) for the 100 W sample was lower compared to the samples at 150 W and 200 W. This lower R^2 value indicates a poorer fit for the kinetic models at this power level, suggesting that the adsorption process may be more heterogeneous and less predictable at lower ultrasonic power. Additionally, there was no clear trend observed for the rate constant k_1 in the PFOK model across different power levels. This lack of trend could be due to the complex interplay between ultrasonic power, particle size, and surface characteristics, which collectively influence the adsorption kinetics. The variability in k_1 values suggests that factors other than just ultrasonic power, such as particle agglomeration and the resulting surface area changes, significantly impact the adsorption dynamics.

Pb(II) adsorption kinetics on magnesia nanomaterials were analyzed using pseudo-second-order kinetics (PSOK) and pseudo-first-order kinetics (PFOK) models. The mathematical expressions for these models are given below Equations (6) and (7):

Pseudo-first-order kinetic model (PFOK):

$$\frac{dQ_t}{dt} = k1(Q_e - Q_t) \tag{6}$$

where Q_t is the amount of Pb(II) adsorbed at time t (mg/g), Q_c is the amount of Pb(II) adsorbed at equilibrium (mg/g), and k_1 is the rate constant of the pseudo-first-order model (1/min).

Pseudo-second-order kinetic model (PSOK):

$$\frac{dQt}{dt} = k2(Q_e - Q_t)^2 \tag{7}$$

where Qt is the amount of Pb(II) adsorbed at time t (mg/g), Q_e is the amount of Pb(II) adsorbed at equilibrium (mg/g), and k_2 is the rate constant of the pseudo-second-order model (g/mg·min).

The data fitting using PFOK and PSOK models showed that the pseudo-second-order kinetic model provided a better fit for the adsorption data compared to the pseudo-first-order model. This conclusion is based on the higher correlation coefficient (R^2) values obtained for the PSOK model (Table 3). Specifically, the R^2 values for the PSOK model were 0.9467, 0.9784, and 0.9937 for ultrasonic powers of 100 W, 150 W, and 200 W, respectively, indicating a good fit. In contrast, the PFOK model showed lower R^2 values, indicating a less accurate fit to the experimental data. The appropriateness of the PSOK model suggests that the adsorption of Pb(II) onto MgO nanomaterials is more consistent with chemisorption processes involving valence forces through sharing or exchange of electrons between adsorbent and adsorbate. Therefore, it can be concluded that the pseudo-second-order kinetic model is more suitable for describing the adsorption kinetics of Pb(II) on MgO nanomaterials in this study.

Table 3. Fitting results estimated by using PFOD and PSOK models.

Ultrasonic Power	PFOK Model			PSOK Model		
	q_e/(mg·g^{-1})	K_1 (1/min)	R^2	q_e/(mg·g^{-1})	K_2 (1/min)	R^2
100 W	36.15	2.17	0.8698	41.69	0.076	0.9467
150 W	27.31	1.09	0.9418	31.97	0.071	0.9784
200 W	22.28	1.71	0.9869	27.34	0.047	0.9937

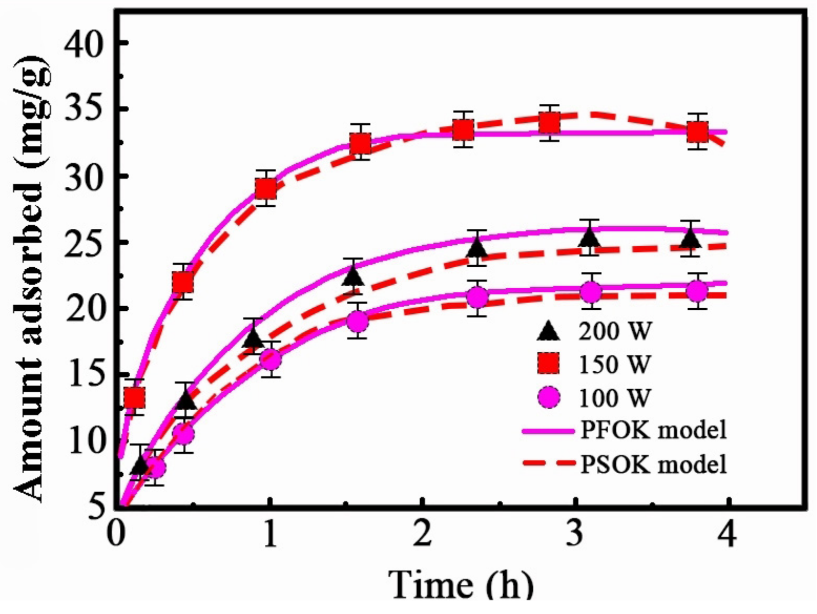

Figure 6. Adsorption kinetics curves of MgO nanomaterials obtained at different ultrasonic powers.

3.6. Impact of Various Temperatures on Adsorption Characteristics

As demonstrated in Figure 7, the effectiveness of Pb(II) adsorption by magnesia nanomaterials synthesized with varying ultrasonic powers was examined at 50 mg/L of Pb(II), pH 4.5, with 20 min being the optimal reaction time. Their adsorption capability for Pb(II) increased gradually from 0 °C to 30 °C. This occurrence can be ascribed to the rise in energy levels at the active sites on the adsorbent's surface at higher temperatures, thereby facilitating the adsorption reaction. Furthermore, higher temperatures improved the thermal mobility of magnesia nanomaterial molecules and Pb(II) ions, thereby increasing the number of collisions and accelerating the adsorption process. It is worth mentioning that the capacity of magnesia nanoparticles for Pb(II) adsorption decreased for temperatures exceeding 30 °C. This occurrence could be elucidated by three distinct factors. First, adsorption is an inherently reversible dynamic equilibrium process, which exhibits greater prominence at lower temperatures. With increasing temperature, the detachment of adsorbents from their surface into the solution intensifies, resulting in decreased adsorption [24]. Second, higher temperatures speed up ion migration, promoting Pb(II) desorption from adsorption sites. Finally, increasing the temperature disrupts the adsorption reaction's chemical equilibrium, thereby lowering the adsorption capacity. Thus, in the 10 °C to 40 °C temperature range, magnesia nanomaterials were discovered to be particularly effective at removing Pb(II). Magnesia nanoparticles produced at an ultrasonic power of 150 W compared to those prepared with 100 W and 200 W exhibited the maximum adsorption capacity (68.94 mg/g).

The effect of temperature on the adsorption capacity of Pb(II) by MgO nanomaterials was investigated at different temperatures (Figure 7). The experiments were conducted at pH 4.5 to simulate slightly acidic conditions commonly found in industrial wastewater. To understand the thermodynamic parameters, the adsorption data were analyzed using the Van't Hoff Equation (8):

$$\Delta G^0 = \Delta H^0 - T\Delta S^0 \tag{8}$$

where ΔG^0 is the Gibbs free energy change, ΔH^0 is the enthalpy change, ΔS^0 is the entropy change, and T is the temperature in Kelvin. The Gibbs free energy change ΔG^0 was calculated using Equation (9):

$$\Delta G^0 = -RT\ln K_c \tag{9}$$

where R is the universal gas constant (8.314 J/mol·K), and K_c is the equilibrium constant of the adsorption process. The values of ΔH^0 and ΔS^0 were determined from the slope and intercept of the Van't Hoff plot of $\ln K_c$ versus $1/T$.

The thermodynamic parameters are summarized in Table 4. The negative values of ΔG^0 at different temperatures indicate that the adsorption process is spontaneous. The positive value of ΔH^0 suggests that the adsorption is endothermic, while the positive value of ΔS^0 indicates an increase in randomness at the solid–liquid interface during the adsorption of Pb(II) ions.

The effect of temperature on the adsorption kinetics was evaluated by conducting adsorption experiments at different temperatures (30 °C, 40 °C, 50 °C) and analyzing the data using the pseudo-second-order kinetic model, which was previously determined to be the most appropriate model for this system. The rate constants k_2 and the adsorption capacities q_e at different temperatures are presented in Table 5. The results show that both the rate constant and the adsorption capacity increase with temperature, indicating that higher temperatures enhance the adsorption rate and the overall adsorption capacity. This can be attributed to increased molecular motion and diffusion rates at higher temperatures, which facilitate the interaction between Pb(II) ions and the active sites on the MgO nanomaterial surface.

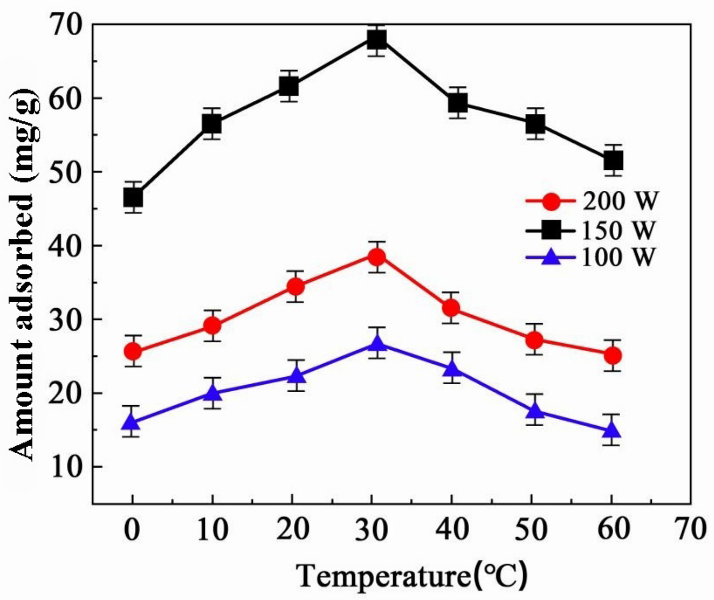

Figure 7. Impact of various temperatures on adsorption characteristics of MgO nanomaterials.

Table 4. Thermodynamic parameters for the adsorption of Pb(II) on MgO nanomaterials.

Temperture (K)	ΔG^0 (KJ/mol)	ΔH^0 (KJ/mol)	ΔS^0 (J/mol·K)
303	−5.23	21.75	89.40
313	−6.21	66	
323	−7.10	16	

Table 5. Kinetic parameters for the adsorption of Pb(II) on MgO nanomaterials at different temperatures using the pseudo-second-order model.

Temperture (°C)	q_e (mg/g)	k_2 (g/mg·min)	R^2
30	31.97	0.071	0.9784
40	35.42	0.084	0.9832
50	38.56	0.097	0.9879

3.7. Isothermal Adsorption

The adsorption capacity of magnesia nanoparticles produced using three distinct ultrasonic powers was investigated in this work. The following are the experimental conditions used for the analysis: pH 6.0, 50 mg/L initial Pb(II) concentration, 30 °C temperature, and the optimal time for the adsorption reaction is 2 h. Figure 8 shows a distinct correlation between the adsorption capability of magnesia nanomaterials and the equilibrium Pb (II) concentration. Increasing the ultrasonic power during the production process greatly enhances their adsorption capability for Pb(II). Specifically, at equilibrium concentrations of 50–100 mg/L, the adsorption efficiency is considerably improved. The adsorption rate gradually increased beyond 100 mg/L until an equilibrium state was achieved. This effect arises from the abundance of unsaturated active sites present on magnesia nanomaterial surfaces during the initial stages of adsorption. The rate of reaction and the strength of Pb(II) binding to magnesia nanoparticles' surface were both improved with increasing Pb(II) concentration. The adsorbent's surface active sites became gradually saturated with an increase in Pb(II) concentration, even though the amount of magnesia nanoparticles remained constant. Therefore, the adsorption capacity increased slowly until it achieved equilibrium.

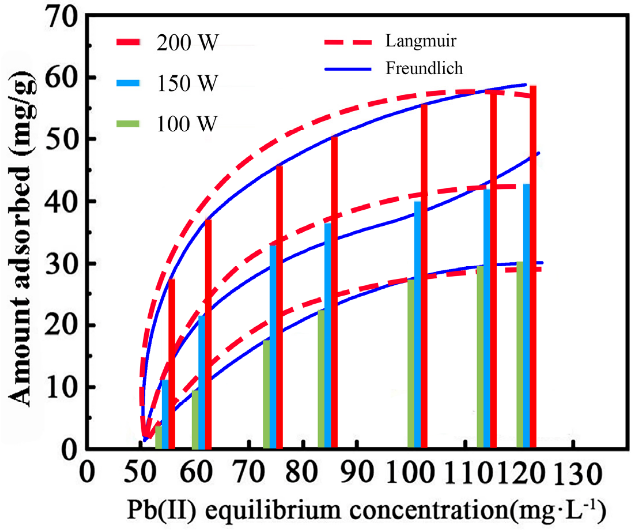

Figure 8. Adsorption isotherm curves of MgO nanomaterials for Pb(II).

The equilibrium adsorption data was analyzed using Freundlich isotherms and Langmuir models to further examine the interaction between magnesia nanomaterials and Pb(II) is presented in Table 6. The Langmuir model provided a perfect fit for the magnesia adsorption behavior for Pb(II), as shown in Table 6, with a correlation coefficient greater than 0.99. According to the findings, monolayer adsorption was identified as the primary mechanism by which Pb(II) is adsorbed onto magnesia nanomaterial. When investigating the impact of ultrasonic power on the magnesia nanomaterial adsorption, the magnesia produced at 150 W exhibited the most significant adsorption of Pb(II), and it was found to have the maximum affinity constant KL at the same time on the surface of magnesia. According to the findings, the KL value rose as ultrasonic power increased, implying that the higher ultrasonic power increased the affinity of magnesia nanomaterials for Pb(II) ions [25].

Table 6. Langmuir and Freundlich model fitting for adsorption of Pb(II) by MgO nanomaterials.

Ultrasonic Power	Langmuir Model			Freundlich Model		
	$Q/(mg{\cdot}g^{-1})$	K_L	R^2	$K_f/(mg{\cdot}g^{-1})$	n	R^2
100 W	65.61	0.057	0.9915	8.57	2.62	0.9571
150 W	53.18	0.036	0.9972	5.40	2.21	0.9640
200 W	37.29	0.029	0.9941	2.95	2.08	0.9756

The equilibrium adsorption data were analyzed using the Freundlich and Langmuir isotherm models. The mathematical expressions for these models are given below in Equations (10) and (11):

Langmuir isotherm model:

$$Q_e = \frac{Q_{max} K_L C_e}{1 + K_L C_e} \tag{10}$$

where Q_e is the amount of Pb(II) adsorbed at equilibrium (mg/g), Q_{max} is the maximum adsorption capacity (mg/g), K_L is the Langmuir constant (L/mg), and C_e is the equilibrium concentration of Pb(II) in solution (mg/L).

The linear plots of $\frac{C_e}{Q_e}$ versus C_e for different ultrasonic powers are shown in Figure 8. The Langmuir constants Q_{max} and K_L were determined from the slope and intercept of the linear plots and are presented in Table 6.

Freundlich isotherm model:

$$Q_e = K_F C_e^{1/n} \tag{11}$$

where Q_e is the amount of Pb(II) adsorbed at equilibrium (mg/g), K_F is the Freundlich constant ((mg/g)(L/mg)^(1/n)), C_e is the equilibrium concentration of Pb(II) in solution (mg/L), and n is a constant related to the adsorption intensity.

3.8. Impact of Various pH on Adsorption Characteristics

The removal rate of magnesia materials produced by ultrasonic electrodeposition at various powers and pH conditions (2.0–10.0) was the subject of a comprehensive investigation to evaluate the influence of various experimental settings on the effectiveness of magnesia materials in adsorbing Pb(II), as illustrated in Figure 9a. The pH_zpc is crucial as it represents the pH at which the surface of magnesium oxide has a neutral charge [26]. MgO was suspended in solutions with different initial pH values, and the final pH was measured after equilibrium. The pH_zpc is the point where the final pH equals the initial pH, indicating that the MgO particle surface has no net charge. The ΔpH value is the difference between the initial pH and the final pH. The mechanism of Pb(II) adsorption mediated by magnesia materials is illustrated in Figure 9b. Magnesia produced $Mg(OH)_2$ upon exposure to water, which was subsequently dissociated simultaneously into OH^-. The pH value of the solution showed a continual increase when the OH^- production rate exceeded the adsorption rate. The solution was gradually neutralized when the OH^- content in the solution reached a critical state and the maximal adsorption rate exceeded the rate of formation. The reaction between O^{2-}, Pb(II), and Mg^{2+} on the magnesia surface forms $MgPbO_3$, which contributes to the abrupt decrease in the removal rate. Furthermore, carbonate formation further hindered the adsorption process.

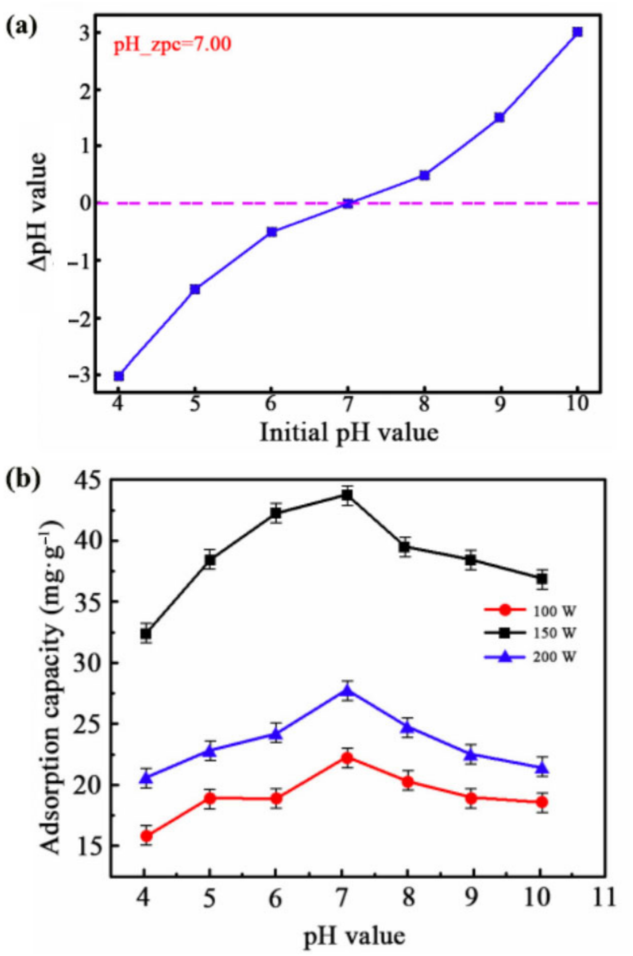

Figure 9. Impact of various pH on adsorption characteristics: (**a**) pH value and pH_zpc, (**b**) adsorption capacity of MgO nanomaterials.

3.9. Impact of Various pH on Adsorption Characteristics

MgO nanomaterials interact with water molecules during adsorption to form $Mg(OH)_2$ [27]. Figure 10 shows the FTIR spectra of MgO nanomaterials synthesized under varying ultrasonic powers for Pb(II) adsorption. The spectra reveal several characteristic peaks, indicating differences in surface functional groups and the interaction strength between Pb(II) and MgO. The prominent peak at 3542 cm^{-1} corresponds to the A_{2u} (OH) lattice stretching vibration, found in pure MgO, suggesting a high concentration of surface hydroxyl groups. As ultrasonic power increases, the intensity of this peak diminishes, indicating a possible decrease in hydroxyl content on MgO's surface. The consistent peak at 1753 cm^{-1} across all samples is associated with water molecule bending vibrations, reflecting their involvement in the adsorption process. The peak broadening between 1479 cm^{-1}, which becomes more pronounced with higher ultrasonic power, is attributed to bicarbonates forming on MgO's surface due to $Mg(OH)_2$ reacting with atmospheric CO_2. Significant surface structure changes at higher ultrasonic powers are evidenced by the peak shift at 968 cm^{-1}. Additionally, a distinct peak at 733 cm^{-1}, most pronounced at 100 W ultrasonic power, corresponds to Pb-O lattice vibrations, indicating the formation of magnesium plumbate as Pb(II) interacts with $Mg(OH)_2$. This observation aligns with the Pb-O lattice seen in the Na_2O_3Pb FTIR spectrum, supporting the idea that Pb(II) removal by MgO nanomaterials results from a chemical reaction with $Mg(OH)_2$.

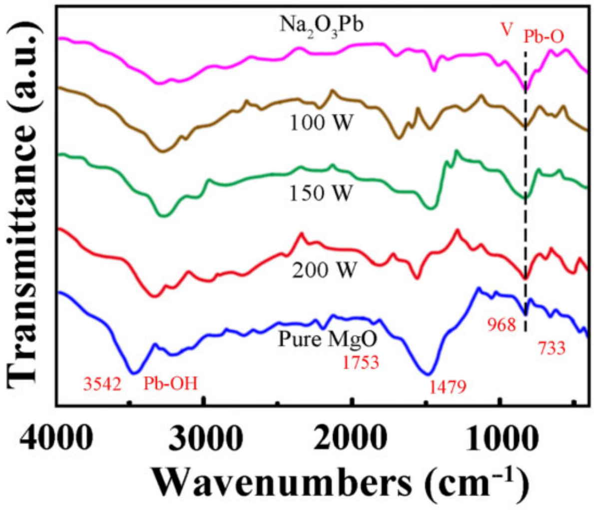

Figure 10. FTIR spectra of the MgO nanowires before and after Pb(II) adsorption with an increased ultrasonic power.

4. Conclusions

(1) Ultrasonic electrodeposition with different strengths and high-temperature heating were used to prepare magnesia nanoparticles. The TEM and SEM analyses showed that the magnesia nanomaterials developed using an ultrasonic power of 150 W demonstrated a porous structure, an even distribution, and approximately 300 nm particle size.

(2) The XRD and BET studies revealed that the adsorption capacity of magnesia nanoparticles increased to 68.94 $mg \cdot g^{-1}$ for Pb(II) in a leaded solution at 150 W. Furthermore, the FTIR analysis suggested the Pb(II) chemisorption by magnesia material.

(3) The most effective adsorption performance and remarkable pH compatibility were observed at 30 °C for magnesia nanoparticles produced with 150 W ultrasonic power. The adsorption procedure was carried out following PSOK, employing a Langmuir-based monolayer chemical adsorption mechanism.

Author Contributions: Methodology, D.T.; Conceptualization, Q.Z.; Validation and Investigation, G.T.; Resources, L.H.; Writing—original draft, F.X. All authors have read and agreed to the published version of the manuscript.

Funding: The research is supported by the Liaoning Provincial Engineering Research Center for High-Value Utilization of Magnesite (LMNY2024020208), the Liaoning Provincial Key Laboratory of Energy Storage and Utilization (CNNK202317), the Liaoning Provincial Engineering Research Center for High-Value Utilization of Magnesite (LMNKY202309\LMNKY202310), the Liaoning Provincial Engineering Research Center for High-Value Utilization of Magnesite (LMNKZ202303), the Yingkou Institute of Technology's Introduction of Talents and Scientific Research Startup Project (YJRC202019), and the Liaoning Regional Joint Fund Project (2022-YKLH-15).

Institutional Review Board Statement: Not applicable.

Informed Consent Statement: Not applicable.

Data Availability Statement: Data are contained within the article.

Conflicts of Interest: The authors declare no conflicts of interest.

References

1. Tian, Y.X.; Zhang, H.; Pan, S.C.; Yin, Y.B.; Jia, Z.Y.; Zhou, H.F. Amine-functionalized magnetic microspheres from lignosulfonate for industrial wastewater purification. *Int. J. Biol. Macromol.* **2023**, *224*, 133–142. [CrossRef] [PubMed]
2. Huang, Y.F.; Li, Y.; Yan, J.; Yan, X.P. Magnetic immobilization of amine-functionalized magnetite microspheres in a knotted reactor for on-line solid-phase extraction coupled with ICP-MS for speciation analysis of trace chromium. *J. Anal. At. Spectrom.* **2010**, *25*, 1467–1474. [CrossRef]
3. Savun-Hekimoglu, B.; Isler, Z.; Hekimoglu, M.; Burak, S.; Karli, D.; Yucekaya, A.; Akpinar, E.; Ediger, V.S. Optimization of wastewater treatment systems for growing industrial parks. *Sci. Total Environ.* **2023**, *905*, 167223. [CrossRef] [PubMed]
4. Shaema, A.; Mangla, D.; Shehnaz; Chaudhry, S.A. Recent advances in magnetic composites as adsorbents for wastewater remediation. *J. Environ. Manag.* **2022**, *306*, 114483.
5. Zhao, B.Y.; He, J.J.; Wang, L. Adsorption/desorption performance of cellulose membrane for Pb (II). *Green Process. Synth.* **2023**, *12*, 20230014. [CrossRef]
6. Desalegn, Y.M.; Andoshe, D.M.; Desissa, T.D. Composite of bentonite/$CoFe_2O_4$/hydroxyapatite for adsorption of Pb (II). *Mater. Res. Express* **2021**, *7*, 115501. [CrossRef]
7. Azzaz, A.A.; Jellali, S.; Akrout, H.; Assadi, A.A.; Bousselmi, L. Dynamic investigations on cationic dye desorption from chemically modified lignocellulosic material using a low-cost eluent: Dye recovery and anodic oxidation efficiencies of the desorbed solutions. *J. Clean. Prod.* **2018**, *201*, 28–38. [CrossRef]
8. Tomishige, K.; Chen, Y.; Li, X.; Yokoyama, K.; Fujimoto, K. Development of active and stable nickel-magnesia solid solution catalysts for CO_2 reforming of methane. *Stud. Surf. Sci. Catal.* **1998**, *114*, 375–378.
9. Jayapriya, M.; Premkumar, K.; Arulmozhi, M.; Karthikeyan, K. One-step biological synthesis of cauliflower-like Ag/MgO nanocomposite with antibacterial, anticancer, and catalytic activity towards anthropogenic pollutants. *Res. Chem. Intermed.* **2020**, *46*, 1771–1788. [CrossRef]
10. Ma, C.; He, H.; Xia, F.; Xiao, Z.; Liu, Y. Performance of Ni-SiC composites deposited using magnetic-field-assisted electrodeposition under different magnetic-field directions. *Ceram. Int.* **2023**, *49*, 35907–35916. [CrossRef]
11. Akbarpour, M.; Asl, F. Fabrication of high-performance graphene/nickel-cobalt composite coatings using ultrasonic-assisted pulse electrodeposition. *Ceram. Int.* **2023**, *49*, 13829–13835. [CrossRef]
12. Zhang, Z.; Feng, R.; Li, R.; Gong, J.; Jiang, C.; Yang, R.; Feng, M.; Pan, Y.; Wang, X. Effect of ultrasonic field on the mechanism of electrodeposited Cu nucleation and growth. *J. Mater. Res. Technol.* **2023**, *26*, 32–41. [CrossRef]
13. Chen, Y.; Li, H.; Zhu, J.; Fang, C.; Li, Z.; Jiang, W. Fabrication of Ni-TiN nanocomposite coatings by ultrasonic assisted jet electrodeposition. *Proc. Inst. Mech. Eng. Part B J. Eng. Manuf.* **2023**. [CrossRef]
14. Li, H.; Zhang, Y.; Li, C.; Tian, Q. Effects of ultrasonic power on the electrochemical characteristics of high-performance nanosized zinc-cobalt oxide electrodes for asymmetric supercapacitors. *Ceram. Int.* **2024**, *50*, 29620–29631. [CrossRef]
15. Liu, J.K.; Yang, L.J.; Song, Z.L.; Xu, C. Microstructures and capacitance performance of MnO_2 films fabricated by ultrasonic-assisted electrodeposition. *Appl. Surf. Sci.* **2019**, *478*, 94–102. [CrossRef]
16. Rajput, M.S.; Pandey, P.M.; Jha, S. Fabrication of nano-sized grain micro features using ultrasonic-assisted jet electrodeposition with pulsed current supply. *Proc. Inst. Mech. Eng. Part B-J. Eng. Manuf.* **2014**, *11*, 1338–1349. [CrossRef]
17. Rakanovic, M.; Vukojevic, A.; Savanovic, M.M.; Armakovic, S.; Pelemis, S.; Zivic, F.; Sladojevic, S.; Armakovic, S.J. Zeolites as Adsorbents and Photocatalysts for Removal of Dyes from the Aqueous Environment. *Molecules* **2022**, *27*, 6582. [CrossRef]
18. Coulibaly, G.N.; Rtimi, S.; Assadi, A.A.; Hanna, K. Nano-sized iron oxides supported on polyester textile to remove fluoroquinolones in hospital wastewater. *Environ. Sci.-Nano* **2020**, *7*, 2156–2165. [CrossRef]
19. Kim, J.; Coulibaly, G.N.; Yoon, S.; Assadi, A.A.; Hanna, K.; Bae, S. Red mud-activated peroxymonosulfate process for the removal of fluoroquinolones in hospital wastewater. *Water Res.* **2020**, *184*, 116171. [CrossRef]
20. Li, X.L.; Tang, G.; Zhang, D.; Wu, L.J.; Lu, S.J.; Zhang, Y.Z.; Cao, X.; Cheng, W.; Feng, J.T.; Yan, W.; et al. Fouling control in ultrafiltration of secondary effluent using polyaniline/TiO_2 adsorption and subsequent treatment of desorption eluate using electrochemical oxidation. *Chem. Eng. J.* **2020**, *382*, 122915. [CrossRef]

21. Tognotti, L.; Flytzani-Stephanopoulos, M.; Sarofim, A.F.; Kopsinis, H.; Stoukides, M. Study of adsorption-desorption of contaminants on single soil particles using the electrodynamic thermogravimetric analyzer. *Environ. Sci. Technol.* **1991**, *25*, 104–109. [CrossRef]
22. Mahmoud, H.R.; El-Molla, S.A.; Naghmash, M.A. Novel mesoporous MnO_2/SnO_2 nanomaterials synthesized by ultrasonic-assisted co-precipitation method and their application in the catalytic decomposition of hydrogen peroxide. *Ultrasonics* **2019**, *95*, 95–103. [CrossRef]
23. Mahmood, T.; Saddique, M.T.; Naeem, A.; Mustafa, S.; Zeb, N.; Shah, K.H.; Waseem, M. Kinetic and thermodynamic study of Cd(II), Co(II) and Zn(II) adsorption from aqueous solution by NiO. *Chem. Eng. J.* **2011**, *171*, 935–940. [CrossRef]
24. Peltier, F.; Thierry, D. Review of Cr-free coatings for the corrosion protection of aluminum aerospace alloys. *Coatings* **2022**, *12*, 518. [CrossRef]
25. Javani, R.; Maghsoudi, H.; Gilan, S.D.; Majidpour, M. Study on adsorption performance of different adsorbents in nitrogen/methane separation. *Sep. Sci. Technol.* **2020**, *56*, 2562–2577. [CrossRef]
26. Deb, A.; Debnath, A.; Saha, B. Sono-assisted enhanced adsorption of eriochrome Black-T dye onto a novel polymeric nanocomposite: Kinetic, isotherm, and response surface methodology optimization. *J. Dispers. Technol.* **2020**, *42*, 1579–1592. [CrossRef]
27. Doweidar, H.; El-Damrawi, G.; Mansour, E.; Fetouh, R.E. Structural role of MgO and PbO in MgO-PbO-B_2O_3 glasses as revealed by FTIR; a new approach. *J. Non-Cryst. Solids* **2012**, *358*, 941–946. [CrossRef]